Tunable competing magnetic anisotropies and spin reconfigurations in ferrimagnetic math xmlns="http://www.w3.org/1998/Math/MathML">mrow>msub>mi>Fe/mi>mrow>mn>100/mn>mo>−/mo>mi>x/mi>/mrow>/msub>msub>mi>Gd/mi>mi>x/mi>/msub>/mrow>/math> alloy films

A. Chanda, J. E. Shoup, N. Schulz, D. A. Arena, and H. Srikanth

Phys. Rev. B **104**, 094404 — Published 1 September 2021

DOI: 10.1103/PhysRevB.104.094404

Tunable competing magnetic anisotropies and spin reconfigurations in ferrimagnetic $Fe_{100-x}Gd_x$ alloy films

A. Chanda, J. E. Shoup, N. Schulz, D. A. Arena and H. Srikanth[1]

Department of Physics, University of South Florida, Tampa, Florida 33620

Abstract

We report a comprehensive study of the temperature evolution of in-plane (IP) and out-of-plane (OOP) effective magnetic anisotropies in compensated ferrimagnetic $Fe_{100-x}Gd_x$ alloy films by employing DC magnetometry and radio frequency (RF) transverse susceptibility measurements. We suggest that our $Fe_{100-x}Gd_x$ system is chemically inhomogeneous and phase segregates into Fe-enriched and Gd-enriched regions. Our IP and OOP magnetometry results indicate that the system undergoes a temperature-driven transformation from an IP spin configuration-dominated state to an OOP spin configuration-dominated state below a certain temperature (spin reorientation temperature). A two-step reversal behavior emerges in the OOP M(H) loop near compensation, which we attribute to the sequential magnetization reversals of Fe-enriched and Gd-enriched domains. Field-induced spin-flop transitions were also observed near the compensation. Our RF transverse susceptibility (TS) measurements indicate that the effective magnetic anisotropy for OOP configuration dominates over that for IP configuration below a certain spin reorientation temperature. Both IP and OOP anisotropy fields determined from our TS measurement exhibit a

[1] Author for correspondence: sharihar@usf.edu

minimum around the compensation temperature which has been explained in the framework of the Stoner-Wohlfarth model.

I. INTRODUCTION

Antiferromagnets serve as a promising alternative to ferromagnets due to their potential for spintronic applications, as their highly stable antiparallel spin configuration produces negligible stray fields. Particularly interesting are ferrimagnetic materials as they bring together some of the compelling features of both ferromagnets and antiferromagnets. Recently, there has been a resurgence of interest in rare earth (RE)-transition metal (TM) ferrimagnetic thin films with perpendicular magnetic anisotropy (PMA) because of their prospects for wide-ranging magneto-optical[1] and spintronic applications including, ultrafast light-controlled magnetic switching[2,3], heat-assisted magnetic recording/thermomagnetic switching [4-6], spin-orbit torque driven magnetization switching[7-9], multilevel current-induced switching[10], THz emission[11], and even for hosting stable topological spin textures [12,13]. This fascinating class of materials has been well known for decades due to their intriguing magnetic properties including PMA.[14-16] Another remarkable characteristic of the RE-TM family is the temperature-tuned spin reorientation transition stemming from the competition between PMA and in-plane shape anisotropy.[17,18] Several mechanisms have been proposed in the past few years to attempt to understand the physical origin of PMA in amorphous RE-TM ferrimagnetic films namely, the RE single-ion anisotropy[19], exchange anisotropy[20], magnetoelasticity induced bond-orientation anisotropy[21], pair ordering originating from magnetic dipolar interactions between anisotropically distributed atomic moment pairs[22], anisotropic pair-pair correlations[23], and most recently, nanoscale chemical phase segregation[24].

Similar to other members of the RE-TM based ferrimagnetic films, the FeGd amorphous ferrimagnetic films also provide flexibility to tune the saturation magnetization, coercive field, magnetic anisotropy, and compensation temperature by varying the chemical composition. [25,26] In addition, the FeGd amorphous films possess a reasonably large magnetic moment in both of the sublattices and exhibit excellent laser induced composition temperature switching which makes this system a potential candidate for magneto-optical recording.[27] While other members of the RE-TM family, for example, Tb based RE-TM systems exhibit weak exchange coupling between the Tb and TM sublattice giving rise to a broad orientational distribution of the RE moment often termed sperrimagnetism, the Gd moments are strongly exchange coupled to the Fe moments in FeGd systems giving rise to a stable collinear ferrimagnetic spin configuration at low fields.[28] Moreover, compared to the RE-Co based films, e.g., TbCo, the saturation magnetization of FeGd amorphous films is weakly dependent on the Argon pressure.[29] All these features make the $Fe_{100-x}Gd_x$ amorphous films particularly attractive from both a fundamental and application point of view. Magnetic properties of single-layer $Fe_{100-x}Gd_x$ alloy films[30-32], as well as Fe/Gd multilayer heterostructures[33,34] have been extensively investigated over the past few years. Depending on the temperature and applied magnetic field strength, both single layer and multilayer films exhibit exotic magnetic phases. Since the ordering temperatures of Fe and Gd are significantly different ($T_C^{Fe} \approx 1043\ K$ and, $T_C^{Gd} \approx 293\ K$), the ordering temperature of $Fe_{100-x}Gd_x$ alloy and Fe/Gd multilayer films lies between T_C^{Fe} and T_C^{Gd} because of strong exchange coupling between Fe and Gd sublattices. However, upon lowering temperature, the magnetization of Gd-sublattice increases more steeply than Fe-sublattice; because of this there exists a compensation temperature (T_{Comp}) at which the Fe-sublattice magnetization (M_{Fe}) cancels out the Gd-sublattice magnetization (M_{Gd}). It is known that $M_{Fe} > M_{Gd}$ for $T > T_{Comp}$, and $M_{Gd} > M_{Fe}$ for $T < T_{Comp}$.[34] According to the (H, T) phase diagram constructed by Camley *et al.*,[35] for Fe/Gd multilayers, when the applied field (H_{DC}) strength is lower than a certain critical value, the system transforms from the Fe-aligned state ($M_{Fe} \parallel H_{DC}$) for $T > T_{Comp}$ to the Gd-aligned state ($M_{Gd} \parallel H_{DC}$) for $T < T_{Comp}$. If H_{DC} exceeds the critical value, the collinear Gd-aligned (Fe-aligned) state for $T < T_{Comp}$ ($T > T_{Comp}$) transforms into a non-collinear metastable state, also known as the "twisted state"[35]. The occurrence of such field-induced phase transformation suggests the existence of spin-flop transition in these systems.[36] The emergence of such spin-flopped state has also been observed in $Fe_{100-x}Gd_x$ amorphous films via Hall measurements [37]. Moreover, the $Fe_{100-x}Gd_x$ amorphous films exhibit excellent PMA for certain composition range[38-40], the origin of which cannot be explained by pair ordering mechanism as Gd does not possess single ion magnetic anisotropy[41]. Most recently, by exploiting SQUID-VSM magnetometry, scanning transmission x-ray microscopy (STXM), and scanning transmission electron microscopy equipped with energy-dispersive x-ray spectroscopy (STEM-EDX), Kirk et al.,[24] showed the presence of nanoscale chemical phase segregation in the FeGd amorphous films; this leads to the formation of Gd-enriched columnar domain structures with out-of-plane (OOP) anisotropy surrounded by Fe-enriched regions with in-plane (IP) anisotropy. They showed that it is possible to tune the competing anisotropies by changing the film thickness, which in turn tailors the spin reorientation transition. To better understand the PMA, spin reorientation temperature window in $Fe_{100-x}Gd_x$ amorphous films, and to manipulate these properties for efficient magneto-optical and spintronic applications, a comprehensive study of the temperature profile of both IP and OOP magnetic anisotropy is indispensable.

In this paper, we have thoroughly investigated the magnetic properties of single-layer ferrimagnetic amorphous thin films of $Fe_{100-x}Gd_x$ ($22.8 \leq x \leq 26.2$) by utilizing vibrating sample magnetometry (VSM) and tunnel diode oscillator (TDO) based radio frequency (RF) transverse susceptibility measurements. RF transverse susceptibility (TS) is a well-known ultra-sensitive technique to precisely determine the effective magnetic anisotropy. It was shown that the compensation temperature can be shifted to a higher temperature by increasing the Gd concentration, which was confirmed by VSM measurements. From IP and OOP magnetometry measurements, we observed that the system undergoes a temperature-driven transformation from an IP spin configuration-dominated state to an OOP spin configuration-dominated state, below a certain temperature (spin reorientation temperature). From the TS measurements performed in both IP and OOP configurations, we have demonstrated for the first time that the effective magnetic anisotropy is higher for the OOP configuration than the IP configuration, below the spin reorientation transition, which strongly agrees with our magnetometry results as well as previous predictions[24,38-40] of PMA in these amorphous $Fe_{100-x}Gd_x$ films. Both IP and OOP anisotropy fields determined from our TS measurement exhibit a minimum around T_{Comp} which has been explained in the framework of the Stoner-Wohlfarth model.

II. EXPERIMENTAL

The samples were grown on a silicon substrate using a combination of DC and RF magnetron sputtering at room temperature in an ultrahigh vacuum deposition chamber with a base pressure of 4×10^{-9} Torr. All the samples have the same nominal structure; Substrate/SiO_z(3nm)/Ta(8nm)/$Fe_{100-x}Gd_x$(80nm)/Ta(6nm). The Gd concentration (x) was varied with the following concentrations, x = 22.8, 24.3, 25.3, and 26.2 (%) and designated as samples A, B, C, and D, respectively. The $Fe_{100-x}Gd_x$ layers were grown by co-sputtering from pure Fe and Gd targets and changing the power of the Gd gun to achieve the variation in the concentration. The composition of the samples was measured using energy-dispersive x-ray spectroscopy (EDS) and has a standard deviation of less than 1%. To obtain the structural profile of the samples we performed low angle X-ray reflectivity (XRR) scans across an angular range of 0°– ~5°.[42] Our XRR results indicate that the $Fe_{100-x}Gd_x$ films are ≈ 750 ± 20Å thick and the Ta cap and seed layers are 60 ±10Å and 75 ±5Å thick. Interfacial roughness at the bottom Ta/$Fe_{100-x}Gd_x$ is 6 ±2Å and the interface between the Ta cap and the $Fe_{100-x}Gd_x$ layer is 33 ±10Å. High-angle X-ray diffraction (XRD) confirmed the amorphous nature of our films.[42]

The in-plane (IP) and out-of-plane (OOP) static magnetic characterization of the samples were performed using a vibrating sample magnetometer (VSM) attached to the physical property measurement system (PPMS) (Quantum Design, Inc., USA). Transverse susceptibility (TS) measurements were performed by making use of a custom-built self-resonant tunnel diode oscillator (TDO) circuit with a resonance frequency of ≈ 12 MHz, and a sensitivity of ≈ 10 Hz. The film was placed inside an inductor (L) coil of the LC tank circuit and incorporated into the PPMS in such a manner that the RF magnetic field (H_{RF}) generated inside the coil is oriented along the plane of the film surface, but transverse to the direction of the external DC magnetic field (H_{DC}) produced by the superconducting magnet of the PPMS. The remaining components of the TDO circuit were accommodated outside the PPMS. Here, the PPMS served as a platform to sweep the DC magnetic field and temperature. Note that the geometry of our experimental setup allows both in-plane ($H_{DC} \parallel$ film surface) and out-of-plane ($H_{DC} \perp$ film surface) configurations; $H_{DC} \perp H_{RF}$ for both configurations. The magnetic field dependence of TS at a fixed temperature was performed by recording the change in the resonant frequency of the LC tank circuit as the H_{DC} was swept from positive to negative saturation and then back to positive saturation. We restricted the

TS measurements to the range of 40 K ≤ T ≤ 300 K as it was difficult to stabilize the coil temperature (and, hence the sample temperature) below 40 K.

III. RESULTS

A. Temperature and magnetic field dependence of magnetization

Fig. 1(a)-(d) display the temperature dependence of the in-plane magnetization, *M*(*T*) of the $Fe_{100-x}Gd_x$ films with different Gd concentrations measured in a magnetic field of μ_0H = 1 T in the temperature range 10 K ≤ T ≤ 350 K. The *M*(*T*) of sample A (lowest Gd concentration) decreases almost monotonically down to the lowest temperature. On the other hand, the *M*(*T*) of sample B also shows a gradual decrease upon cooling, but a broad minimum appears around 70 K, which we identify as the compensation temperature (T_{Comp}). The compensation is more prominent for sample C, and it occurs at a higher temperature (T_{Comp} = 200 K) than sample B, therefore T_{Comp} moves to a higher temperature upon increasing Gd concentration. For sample D with the highest Gd concentration, the compensation point is above the measured range and hence, the *M*(*T*) gradually increases upon cooling down to the lowest temperature.

In the main panels of Figs. 2(a)-(d), we compared the in-plane (IP) and out-of-plane (OOP) M(H) loops at T = 300 K for the films A - D, respectively. A diamagnetic contribution from the SiO_2 substrate was subtracted from all the M(H) loops. Note that the magnetization of the saturated ferrimagnetic macro-spins is indicated as the saturation magnetization, M_S throughout the manuscript. Sample A shows nearly saturated square-shaped hysteresis loops for both IP and OOP configurations. A closer look (inset of Fig. 2(a)) reveals that the OOP M(H) first shows a steep jump near the zero-field followed by a gradual evolution towards the opposite saturation. Such behavior of M(H) was previously observed in Fe/Cr/Gd superlattices with Cr thickness greater than 10 Å, which was attributed to independent magnetization reversals of noninteracting Fe and Gd sublattice magnetizations with different coercive fields.[43] For samples B - D, the IP M(H) loop becomes elongated with an increase in the saturation field limit, whereas the OOP M(H) loop exhibits a nearly square-shaped hysteresis loop with a noticeable and consistent increase in coercivity upon increasing Gd concentration, which is evident from the insets of Figs. 2(b)-(d), respectively. For samples A-C, the magnetization value at $\mu_0H = 1$ T is higher for IP configuration than the OOP configuration. For sample D, the magnetization value at $\mu_0H = 1$ T for the OOP M(H) loop is slightly higher than that for the IP M(H) loop. In the main panel of Figs. 2(e)-(h), we compared the IP and OOP M(H) loops at T = 10 K for samples A-D. The IP M(H) loops are more elongated in shape compared to T = 300 K for samples A-D, whereas the OOP M(H) loops are nearly square-shaped for all the samples (see the insets of Figs. 2(e)-(h) for details). Hence the effective easy direction of magnetization is mostly oriented along the OOP direction at T = 10 K for the films A-D. Moreover, a smaller to negligible difference in the magnetization value at μ_0H = 1 T between the IP and OOP configurations is evident for samples A-C. Moreover, the OOP M(H) loops at T = 10 K exhibit distinct shapes in different samples. While samples A and D exhibit a square OOP hysteresis loop with a single-step reversal, two-step magnetization reversals are observed in samples B and C. This two-step magnetization reversal behavior is more prominent in sample B than sample C. Moreover, it is also evident that the coercive field decreases gradually with increasing Gd concentration at T = 10 K which is more prominent from the insets of Figs. 2(e)-(h).

To understand the evolution of the two-step reversal feature in the OOP M(H), we have investigated the hysteresis loops for all our samples at different temperatures. Figs. 3(a)-(d) depict the plots of the OOP M(H) loops in the temperature range: $10 \leq T \leq 300$ K for the samples A-D, respectively. The OOP M(H) loops for both samples A and D exhibit a mostly square shape for all the temperatures. While sample A shows a significant increase in coercivity with decreasing temperature, a monotonic decrease in coercivity upon reducing the temperature is evident for sample D. However, samples B and C show anomalous temperature evolutions of the OOP M(H) loops. For sample B, the M(H) loop exhibits a single step reversal for $T \geq 200$ K but, the two-step magnetization reversal starts appearing for $T \leq 150$ K and it becomes stronger close to the compensation point. At T = 100 K, a notable feature appears in the M(H) loop; an additional magnetization switching with a minor hysteresis loop around $\mu_0H_{SF} \approx 1$ T which is reproducible for the reverse field cycle. For clarity, the OOP M(H) loops at T = 75 and 100 K for sample B are shown separately in Fig. 4(a). Interestingly, this feature occurs at a lower field strength ($\mu_0H_{SF} \approx 0.8$ T) around the compensation point (T = 75 K) but, the two-step magnetization reversal disappears, and the M(H) loop shows significantly lower coercivity. As the temperature is further reduced below compensation, the magnetization switching behavior at $\mu_0 H_{SF}$ disappears but the two-step magnetization reversal reappears. Similar temperature evolution of the OOP M(H) was also observed in sample C around the compensation temperature T_{Comp} = 200 K. For clarity, the OOP M(H) at T = 200 K is shown separately in Fig. 4(b), which exhibits a magnetization switching accompanied by a minor hysteresis loop around $\mu_0 H_{SF} \approx 0.8$ T, as in sample B. As observed in sample B, this feature at μ_0H_{SF} disappears below the compensation. Although the two-step magnetization reversal reappears below compensation, it fades away below T = 100 K.

In Figs. 5(a)-(d), we show the temperature dependence of saturation magnetization (M_S) normalized with respect to its value at T = 300 K (M_S/M_S^{300K}) on the left vertical-scale and the ratio of remanent magnetization (M_R) and M_S on the right vertical-scale obtained from the OOP M(H) loops for the samples A-D. The ratio M_R/M_S determines the squareness of the hysteresis loop and hence, an important parameter to understand the behavior of magnetic anisotropy. For sample A, which does not show any compensation, M_S/M_S^{300K} initially decreases smoothly up to 150 K and then abruptly decreases down to the lowest temperature, whereas M_R/M_S increases smoothly with decreasing temperature along with a slope change around 150 K. We believe that steep enhancement of Gd-sublattice magnetization for $T \leq 150$ K is responsible for this behavior which also hints that the easy direction of magnetization is tilting towards the OOP orientation. In a sharp contrast to sample A, M_S/M_S^{300K} and M_R/M_S for both samples B and C exhibit minima around their compensation point which is followed by an increase in both these parameters, indicating a strong influence of magnetic anisotropy on the magnetic behavior of these samples around their compensation. In the case of sample D, for which compensation is expected at a higher temperature than both samples B and C, both M_S/M_S^{300K} and M_R/M_S smoothly increase with decreasing temperature which is consistent with a sample with a high compensation temperature. We have also shown the temperature profiles of the coercive field for the OOP configuration (H_C^{OOP}) for the samples A-D in Figs. 5(e)-(h), respectively. While H_C^{OOP} for sample A smoothly increases with decreasing temperature, For Sample B and C, H_C^{OOP} exhibits a sharp minimum around $T = T_{Comp}$ for those samples, respectively. For both samples B and C, H_C^{OOP} decreases steeply as the temperature moves away from the compensation point. Such behavior strongly suggests that a drastic change in anisotropy energy occurs in the vicinity of the compensation point in these films.

B. Transverse susceptibility and temperature dependence of effective magnetic anisotropy

To investigate the behavior of the effective magnetic anisotropy of $Fe_{100-x}Gd_x$ films under the application of IP and OOP DC bias fields, we performed transverse susceptibility measurements by utilizing a tunnel diode oscillator (TDO) - based self-resonant radio frequency (RF) technique. Transverse susceptibility is an extremely sensitive tool to precisely determine the dynamic magnetic response of the material to a small, and fixed amplitude radio frequency (RF) (f = 12 MHz) perturbing magnetic field (H_{RF} ~ 10 Oe) applied perpendicular to a static magnetic field (H_{DC}).[44] The self-resonant circuit consists of an inductor-capacitor (LC) tank circuit and the sample is placed inside the inductor. An application of a dc magnetic field induces a shift in the resonance frequency of the LC tank circuit which provides a direct measurement of the change in inductance and hence, the susceptibility of the sample. In the framework of the Stoner-Wohlfarth (SW) model, if H_{DC} is scanned from positive to negative saturation (and vice versa), the transverse susceptibility (TS) for a single domain particle with uniaxial anisotropy shows sharp peaks at the anisotropy fields, $H_{DC} = \pm H_K$, which is also known as the Aharoni singularity.[45] However, for a system with randomly dispersed magnetic easy axes, the field dependence of TS usually exhibits cusp(s) at the effective anisotropy field(s), $H_{DC} = \pm H_K^{eff}$. Fig. 6(a) represents the 3D polar representation of different orientations of the magnetization vector (M_S), DC, and RF magnetic fields relative to the magnetic easy axis of a single domain particle with uniaxial magnetic anisotropy fulfilling the experimental conditions of a typical TS measurement in the framework of the SW model. Considering the diagram, if H_{DC} and H_{RF} are applied along the z-axis and x-axis respectively, (θ_K, ϕ_K) and (θ_M, ϕ_M) are the (polar, azimuthal) angles of the uniaxial anisotropy axis and the saturation magnetization, M_S, respectively, the TS can be expressed as,[45]

$$\frac{\chi_T}{\chi_0} = \frac{3}{2}\left[cos^2\phi_K \frac{cos^2\theta_M}{hcos\theta_M + cos2(\theta_M - \theta_K)} + sin^2\phi_K \frac{sin(\theta_K - \theta_M)}{hsin\theta_K}\right], \quad (1)$$

where h is the reduced applied field ($h = \frac{H_{DC}M_S}{2K} = \frac{H_{DC}}{H_K}$), and K is the uniaxial anisotropy energy density. For randomly oriented anisotropy axes, the average TS can be expressed as,[45]

$$\left\langle\frac{\chi_T}{\chi_0}\right\rangle = \frac{3}{4}\int_0^{\pi/2}\left[\frac{cos^2\theta_M}{hcos\theta_M + cos2(\theta_M - \theta_K)} + \frac{sin(\theta_K - \theta_M)}{hsin\theta_K}\right] sin\theta_K d\theta_K. \quad (2)$$

Eqn. (2) can be used to numerically calculate the average TS for single-domain SW particles with randomly oriented anisotropy axes. The DC bias field-dependent TS for such systems exhibit sharp peaks at the anisotropy fields, $\pm H_K$ as well as at the switching field (H_{SW}). However, for a system consisting of different regions with distinct anisotropy energy density, the TS probes the effective anisotropy field, H_K^{eff} and the DC bias field-dependent TS exhibits broad maxima centering around $\pm H_K^{eff}$. In that case, it is essential to introduce the magnetic anisotropy field dispersion in the calculations by incorporating a log-normal distribution of the anisotropy fields in the Eqn. (2) with a mean value of $\approx H_K^{eff}$ as,[46,47]

$$\left\langle\widetilde{\frac{\chi_T}{\chi_0}(H_{DC})}\right\rangle = \int_0^\infty \frac{1}{\sqrt{2\pi}\sigma H_K}\left\langle\frac{\chi_T}{\chi_0}\left(\frac{H_{DC}}{H_K}\right)\right\rangle e^{-\frac{1}{2}\left\{\frac{\ln\left(H_K/H_K^{eff}\right)}{\sigma}\right\}^2} dH_K, \quad (3)$$

where σ represents the standard deviation of the quantity $\frac{H_K}{H_K^{eff}}$. The standard deviation of the anisotropy field can thus be expressed as $\sigma_{H_K} = \sigma H_K^{eff}$. Numerical calculations of the TS using Eqn. (3) showed that for unipolar field scans ($+H_{DC}^{sat} \rightarrow -H_{DC}^{sat}$), (a) the peaks associated with the effective anisotropy fields ($\pm H_K^{eff}$) are significantly broadened and (b) the peak heights at $+H_K^{eff}$ and $-H_K^{eff}$ are asymmetric with respect to the zero-field in presence of anisotropy dispersion. These observations were also confirmed experimentally.[46,47]

We have conducted the TS measurements on our $Fe_{100-x}Gd_x$ films at various temperatures in the range 40 K ≤ T ≤ 300 K by saturating them at $\mu_0 H_{DC}^{sat}$ = 3 T for two different orientations of H_{DC}: in-plane (H_{DC} lies along the film surface) and out-of-plane (H_{DC} is perpendicular to the film surface). Note that $H_{DC} \perp H_{RF}$ for both configurations. The schematic of our TS measurement geometry for IP and OOP configurations is shown in Fig. 6(b). Since the TS data were directly obtained from the shift in the resonance frequency of the self-resonant LC tank circuit, we show all the TS in this paper as percentage change, which is defined as, $\frac{\Delta\chi_T}{\chi_T}(\%) = \frac{\chi_T(H_{DC})-\chi_T(H_{DC}^{sat})}{\chi_T(H_{DC}^{sat})} \times 100$, where $\chi_T(H_{DC}^{sat})$ is the value of the transverse susceptibility at the saturation field ($\mu_0 H_{DC}^{sat}$).

Figs. 7(a)-(d) compare the IP and OOP TS data for samples A-D, for bipolar field scans ($+H_{DC}^{sat} \rightarrow -H_{DC}^{sat} \rightarrow +H_{DC}^{sat}$) at T = 300 K. For all the samples, the TS exhibits a broad maximum centering at the effective anisotropy fields: $\pm H_K^{eff}$ for both IP and OOP orientations. Additionally, significant asymmetry in the peak heights at $+H_K^{eff}$ and $-H_K^{eff}$ is visible for all the samples. As previously discussed, these features indicate the presence of anisotropy dispersion in these samples rather than single domain particulate nature with uniaxial anisotropy. For sample A, there is no significant difference between the peak positions in the TS isotherm for IP and OOP orientations of H_{DC}, indicating the almost equal contribution of the IP and OOP spin configurations. This observation is in good agreement with the IP and OOP M(H) hysteresis loops measured on this sample. A large hysteresis in the TS is also notable for both the IP and OOP configurations which is a clear manifestation of the asymmetric peak heights due to anisotropy dispersion. For sample B, the peak heights at $\pm H_K^{eff}$ are almost symmetrical for the IP configuration in sharp contrast to the OOP configuration (the peak heights at $\pm H_K^{eff}$ are identified as $\pm d$). Hence, negligible hysteresis was observed for the IP configuration whereas the hysteresis remains significant for the OOP configuration. On the other hand, the TS curve for sample C exhibits significant hysteresis for both the IP and OOP orientations. Considering the unipolar field scan ($+H_{DC}^{sat} \rightarrow -H_{DC}^{sat}$), the IP TS curve shows a very broad maximum at positive anisotropy whereas the negative anisotropy peak is almost smeared out completely, which signifies very high anisotropy dispersion in the IP orientation. Most importantly, we noticed that the peaks in the TS isotherm occur at higher field values for the IP configuration in comparison to the OOP configuration for both samples B and C. It is to be noted that the maxima observed in the TS scans at $\pm H_K^{eff}$ are associated with the contributions from the spins aligned orthogonal to the direction of H_{DC}.[48] In other words, for the IP configuration, the TS scans probe the dynamics of the OOP spins and vice versa. Hence, the positive peaks in the TS curves for the IP and OOP configurations are identified as the positive OOP effective anisotropy field: $+H_K^{eff,OP}$ = $+H_K^{OP}$ and the positive IP effective anisotropy field: $+H_K^{eff,IP}$ = $+H_K^{IP}$, respectively. Hence, $+H_K^{OP} > +H_K^{IP}$ at T = 300 K for both samples B and C implying IP spin alignment. Conversely, $+H_K^{IP} > +H_K^{OP}$ for sample D at T = 300 K validates our previous argument on the transition from IP to OOP magnetic anisotropy with increasing Gd concentration.

Since samples B and C show compensation within the measured temperature range, we chose to demonstrate the behavior of the IP and OOP TS curves close to their compensation points. In Figs. 7(e)-(h), we compare the IP and OOP TS data for samples A-D, respectively for bipolar field scans at T = 200 K which is the compensation temperature of sample C. In sharp contrast to the TS data observed at T = 300 K (see Fig. 8(a)-(d)), we found that $+H_K^{IP} > +H_K^{OP}$ for all the samples. However, the difference in the IP and OOP effective anisotropy fields, ΔH_K = (H_K^{IP} -

H_K^{OP}) is higher in sample C than the rest of the samples. Another noticeable feature is that the peak heights at positive and negative anisotropy fields are nearly symmetric in the OOP TS curves for all the samples, whereas the IP TS curves show slightly asymmetric peak heights for samples C and D that causes clear hysteresis between $+H_{DC}^{sat} \rightarrow -H_{DC}^{sat}$ and $-H_{DC}^{sat} \rightarrow +H_{DC}^{sat}$ field scans. Similarly, in Figs. 7(i)-(l), we compare the IP and OOP TS data for samples A-D, respectively for bipolar field scans at T = 60 K which is close to the compensation temperature of sample B (T_{Comp} ≈ 70 K). As observed for T = 200 K, $+H_K^{IP} > +H_K^{OP}$ for all the samples, and ΔH_K is higher in sample B than the rest of the samples. Unlike the TS data at T = 200 K, considerable hysteresis is observed between $+H_{DC}^{sat} \rightarrow -H_{DC}^{sat}$ and $-H_{DC}^{sat} \rightarrow +H_{DC}^{sat}$ field scans for the IP configurations for all the samples. This implies anisotropy dispersion is also significant at low temperatures for all the samples, especially for the IP orientation. For sample D, the negative anisotropy peak in the IP TS curve is fully smeared out for $+H_{DC}^{sat} \rightarrow -H_{DC}^{sat}$ field scan. Sample D exhibits an additional remarkable feature in the OOP TS curves at all the temperatures: a sharp peak centering around the zero-field for both $+H_{DC}^{sat} \rightarrow -H_{DC}^{sat}$ and $-H_{DC}^{sat} \rightarrow +H_{DC}^{sat}$ field scans. However, a closer view (see the inset of Fig. 7(l)) reveals the appearance of a peak at -H_{SW} (+H_{SW}) while scanning the field from $+H_{DC}^{sat}$ ($-H_{DC}^{sat}$) $\rightarrow -H_{DC}^{sat}$ ($+H_{DC}^{sat}$). This peak is possibly associated with the switching field. The absence of this feature at $\pm H_{SW}$ for the IP configuration of this sample or both IP and OOP configurations in the other three samples may be because of the broad anisotropy peak which dominates and smears out the switching peak.

IV. DISCUSSION

To summarize the magnetic properties of $Fe_{100-x}Gd_x$ films, we have made two important observations especially for samples B and C around their compensation points. First, as the compensation point is approached, a two-step magnetization reversal behavior starts appearing in the OOP M(H) loop a few Kelvins above and below the compensation temperature. Two-step magnetization reversal has also been observed in a recent study on amorphous FeGd films, where the high field switching was attributed to the Gd-enriched columnar domains with out-of-plane (OOP) anisotropy embedded in Fe-enriched domains with in-plane (IP) anisotropy formed due to partial Fe-diffusion from the FeGd layer to the adjacent Ta layer.[24] Such chemical phase segregation was observed for the films with thickness ≥ 40 nm, but it was absent for film thickness ≤ 20 nm. Chemical phase segregation in RE-TM based amorphous films is not uncommon. For example, Stanciu et al., [49] recently reported the existence of nanoscale phase separation in amorphous $Fe_{100-x}Gd_x$ thin films with thickness between 70-90 nm, particularly for the composition $Fe_{79}Gd_{21}$ which is close to the composition range: $22.8 \leq x \leq 26.2$ for our $Fe_{100-x}Gd_x$ amorphous films with thickness ~ 80-90 nm. Moreover, by making use of magnetic force microscopy (MFM), Basumatary et al., [50] evidenced the presence of magnetically phase separated regions in Tb-Fe amorphous films with strong perpendicular magnetic anisotropy. The thickness of all our films is also ≈ 80 nm, there is a possibility that our system is phase segregated into Fe-rich and Gd-rich regions with different orientations of local anisotropy axes. The two-steps in the OOP M(H) loop observed in samples B and C can thus be explained by sequential magnetization reversals of the Fe-enriched region with low coercivity and Gd-enriched region with higher coercivity. The absence of this behavior in the IP hysteresis loop is consistent with the OOP orientations of the Gd-enriched domains. Since the $Fe_{100-x}Gd_x$ system undergoes a transformation from a high-temperature Fe-aligned state to a low-temperature Gd-aligned state, the Gd-enriched phase plays a dominating role in the vicinity of the compensation as well as at low temperatures. As the Gd-enriched phase prefers an OOP spin configuration, the effective magnetic easy axis also undergoes a transformation from an IP to OOP configuration around the compensation, which indicates the occurrence of spin reorientation in both samples B and C. Increase in the OOP coercivity with increasing Gd concentration is consistent with OOP spin configuration of Gd enriched phase.

In addition to the two-step magnetization reversal, a second magnetization switching behavior accompanied by a minor hysteresis loop appears only within a narrow temperature window around the compensation temperature for samples B and C. In a ferrimagnet alloy such as $Fe_{100-x}Gd_x$, the complexity in the magnetic properties arises from the antiferromagnetic (AFM) exchange coupling between the Fe and Gd sublattices, as well as the distinct temperature profiles of the individual sublattice magnetizations. Like antiferromagnets, it is energetically favorable for a ferrimagnet to align its magnetic easy axis perpendicular to the applied magnetic field. If the magnetic anisotropy is not very strong and a magnetic field is applied parallel to the magnetic easy axis, a competition between Zeeman energy and magnetic anisotropy energy causes a sudden rotation of the two sublattice magnetizations perpendicular to the direction of the applied magnetic field above a certain critical magnetic field. This causes a transformation of the system from an antiparallel collinear spin configuration to a non-collinear canted spin configuration above that critical field. This phenomenon is known as the spin flop (SF) transition, and $\mu_0 H_{SF}$ represents the critical field for SF transition. As per our assumption, our $Fe_{100-x}Gd_x$ system is chemically inhomogeneous and possibly phase segregates into Fe-enriched and Gd-enriched regions. In this framework, we can visualize the SF transition as the flopping of the Fe-enriched and Gd-enriched subnetworks rather than considering the flopping of individual Fe and Gd-sublattices distributed homogeneously throughout the system. According to the two-sublattice model, the resultant saturation magnetization of our ferrimagnetic system at any temperature T can thus be expressed as: $M_S = \left[M_{Gd}^{Rich} - M_{Fe}^{Rich}\right]$; where, M_{Gd}^{Rich} and M_{Fe}^{Rich} are the saturation magnetizations of the Fe-enriched and Gd-enriched subnetworks, respectively. A collinear antiparallel configuration of the sublattice magnetizations persists up to a certain critical value of the external magnetic field $H_{DC} = H_{C,1} = \lambda_{Gd-Fe}^{inh}\left[M_{Gd}^{Rich} - M_{Fe}^{Rich}\right]$; where λ_{Gd-Fe}^{inh} is the molecular field constant associated with the exchange interaction between Fe-enriched and Gd-enriched subnetworks.[51,52] For $H_{DC} \geq H_{C,1}$, the system switches to the SF state that persists in the field range $H_{C,1} \leq H_{DC} \leq H_{C,2}$. A field-induced transformation from the non-collinear canted configuration to a collinear parallel configuration takes place as the applied magnetic field exceeds a second critical field: $H_{DC} \geq H_{C,2} = \lambda_{Gd-Fe}^{inh}\left[M_{Gd}^{Rich} + M_{Fe}^{Rich}\right]$[51,52]. Typically, the values of the critical fields $H_{C,1}$ and $H_{C,2}$ lie in the range of ~ 10 – 100 T. However, at temperatures close to the compensation point, $H_{C,1}$ and $H_{C,2}$ become small and the difference between the critical fields: $\left(H_{C,1} - H_{C,2}\right)$ also become narrow[51,52]. Clearly, $H_{C,1} = 0$ at $T = T_{Comp}$, indicating the appearance of the canted non-collinear state at a much lower field at the compensation temperature. This explains the appearance of the sudden magnetization reversal behavior at $\mu_0 H_{SF}$ in both samples B and C in the vicinity of their compensation points. While decreasing the field from $H_{DC} \geq H_{C,2}$, the transformation from collinear parallel spin configuration to canted SF state occurs at $\approx H_{C,2}^{*} < H_{C,2}$, and upon further decreasing the field, the antiparallel collinear spin configuration is retrieved at $\approx H_{C,1}^{*} < H_{C,1}$, giving rise to a hysteresis around $\mu_0 H_{SF}$.[53] Since the field-induced transition from the collinear antiparallel state to the non-collinear SF state is a first-order metamagnetic transition, such hysteresis is expected.[53,54] It was shown that $H_{C,1}$ and $H_{C,1}^{*}$ are related to the exchange field H_E and anisotropy field H_K at T = 0 K through the relation,[53,55,56]

$$H^*_{C,1} = \left(\frac{2H_E - H_K}{2H_E + H_K}\right) H_{C,1} \quad (4)$$

Eqn. (4) indicates that $H_{C,1} > H^*_{C,1}$, which explains the occurrence of minor hysteresis loop observed around the SF transition in samples B and C in the vicinity of the compensation point. Thermodynamically, the SF transition field is defined as: $H_{SF} = \sqrt{(H_{C,1}.H^*_{C,1})}$.[53] The difference $(H_{C,1} - H^*_{C,1})$ decreases with increasing temperature. For better visibility of the critical fields, we show the expanded OOP M(H) loop for sample B at T = 75 K in Fig. 4(c). The values of $\mu_0 H_{C,1}$, $\mu_0 H_{C,2}$, $\mu_0 H^*_{C,1}$ and $\mu_0 H^*_{C,2}$ are 0.83, 0.91, 0.63, and 0.73 T, respectively and hence, the correct value of $\mu_0 H_{SF}$ = 0.73 T for sample B at T = 75 K. Similarly, the values of $\mu_0 H_{C,1}$, $\mu_0 H_{C,2}$, $\mu_0 H^*_{C,1}$, $\mu_0 H^*_{C,2}$ and $\mu_0 H_{SF}$ are 1.13, 1.22, 0.98, 1.08 T and 1.05 T, respectively at T = 100 K.

Next, we discuss about the difference in IP and OOP saturation magnetization for our $Fe_{100-x}Gd_x$ films. As we can see from the insets of Figs. 2, the difference between the IP and OOP saturation magnetizations is small at low fields whereas the difference increases at higher fields. Krupinski et al.,[41] also observed similar increase in difference between the IP and OOP magnetization values above the low field ferrimagnetic saturation in FeGd amorphous films. Significant difference in IP and OOP saturation magnetization has also been observed in other RE-TM based amorphous ferrimagnetic films.[50,57,58] We believe that the origin of such difference in saturation magnetization value between IP and OOP configurations is related to the spin-flop transition as discussed in the previous section. Below the spin-flop transition, even if the M(H) loop shows tendency of saturation, it is actually not the complete saturation but rather the ferrimagnetic macro-spin saturation. A very high field (~ 10-100 T) is needed to achieve complete saturation where the RE and TM moments are completely aligned. [59] To visualize the entire picture as a function of field, let us consider the "rigid rotation model" for two sublattices in a RE-TM based ferrimagnet [60]. Under the application of a non-zero field (much lower than $H_{C,1}$), the RE and TM sublattice magnetizations are not perfectly antiferromagnetically aligned[60], rather they deviate from the antiparallel alignment by a small angle because of the competition between the Zeeman energy, the exchange energy and the anisotropy energy associated with individual elements. So, the macro-spin consisting of the RE and TM sublattice magnetizations forms a rigid spin-configuration with a very small canting angle, where the canting angle depends on the local anisotropy. When the applied field exceeds $H_{C,1}$, the system transforms from the rigid canted/nearly antiparallel state into the spin-flop state with a larger canting angle between the RE and TM sublattices and, for an applied field $\geq H_{C,2}$, both the sublattice magnetizations re-orient towards the applied field direction and hence, a complete saturation/alignment takes place. Now, let us consider phase segregation as a small perturbation to this scenario. Since there is a possibility that our system is phase segregated into Fe-rich and Gd-rich regions with different orientations of local anisotropy axes, and hence, the canting angles of the rigid $\left[M_{Gd}^{Rich} + M_{Fe}^{Rich}\right]$ macro-spins are different for different phase segregated regions for applied fields $\leq H_{C,1}$. This is possibly the origin of the different values of the ferrimagnetic macro-spin saturation magnetization values for the IP and OOP configurations for our FeGd system when the applied field is smaller than $H_{C,1}$ or, $H_{C,2}$.

The disappearance of the two-step magnetization reversals around the compensation point is expected as the Fe-enriched and Gd-enriched subnetwork magnetizations cancel each other and undergo a transformation to a canted spin-flop state first before flipping their directions simultaneously parallel to the applied field direction rather than independent reversals. Magnetic compensation also strongly influences both squareness of the OOP M(H) loop and coercive force especially in samples B and C. Thus, it seems that magnetic anisotropy plays a crucial role in controlling the magnetic properties of this system, specifically around the compensation temperature. As there may be chemically phase segregated regions, these phases have different easy axes which lead to a competition between local anisotropies and the Zeeman energies, particularly around the global compensation temperature (T_{Comp}). Hence, it is imperative to have a clear understanding of the effective magnetic anisotropy fields as a function of temperature to elucidate the complex magnetic behavior observed in these films around the compensation.

As we already mentioned, the TS scans probe the dynamics of the OOP spins for the IP configuration and vice versa. From our TS measurements, we observed that the effective anisotropy field is higher for the OOP configurations than the IP configurations, *i.e.*, $+H_K^{IP}(T) > +H_K^{OP}(T)$ below the spin reorientation transition (T_{SR}) for samples B and C, and throughout the measured temperature range for sample D. Thus, our TS data is consistent with our magnetometry data. On the other hand, we observed multiple spin reorientation transitions for sample A. Such complex temperature dependence of $+H_K^{IP}$ and $+H_K^{OP}$ suggest that there is a strong competition between the IP and OOP anisotropies in the system. As discussed earlier, for simplicity, we can consider our $Fe_{100-x}Gd_x$ system to be composed of two different anisotropy phases: (1) the Gd-enriched phase which prefers OOP anisotropy, and (2) the Fe-enriched phase that prefers IP anisotropy. The two-step reversal behavior observed in the OOP M(H) at low temperatures indicated the development of the OOP spin configuration in the Gd-enriched phase. Hence, a strong competition between the anisotropies of the Gd-enriched and Fe-enriched regions is expected. Such competing magnetic anisotropies can give rise to anisotropy crossover(s) depending on the dominant contribution, resulting in spin reorientation(s) in the system. Moreover, assuming that our system is most likely phase-segregated into Fe-enriched and Gd-enriched regions, we can expect that different regions have distinct preferred orientations of the magnetic easy axes. Our TS measurements probe the effective anisotropy field which is certainly the average of all local anisotropy axes. This is the origin of anisotropy dispersion in $Fe_{100-x}Gd_x$ system which leads to the observed asymmetry in the peak heights at $+H_K^{eff}$ and $-H_K^{eff}$ as well as broadened peak in the bipolar TS curves for most of the samples shown in Figs. 7.

It is known that the RF transverse susceptibility is the low frequency limit of the ferromagnetic resonance (FMR)[61] and thus it's dynamics follows the Landau-Lifshitz-Gilbert (LLG) equation[62]. In case of FMR, the field dependence of dynamic susceptibility is well-described by Lorentzian function,[63] and hence, the line shapes for the TS curves can also be described by the Lorentzian function, which is expressed as,

$$\frac{\Delta\chi_T}{\chi_T} = A\frac{\left(\frac{\Delta H}{2}\right)^2}{\left(H_{dc}-H_K^{eff}\right)^2+\left(\frac{\Delta H}{2}\right)^2} \quad (5)$$

where, A is the proportionality constant and ΔH is the line width of the TS curves. Similar to FMR, the symmetry of the TS line shape may also depend on the relative phase between RF electric and magnetic field components. When a plane electromagnetic (EM) wave travels through free space, the electric and magnetic field vectors associated with the EM wave are in-phase. However, if the EM wave enters a metallic medium, the electric and magnetic field vectors of the RF wave become out of phase. Since our FeGd system is metallic, the magnetic and electric field vectors associated with the RF EM wave generated by the inductor coil may also become out-of-phase inside the sample. In such case, the resultant TS line shape can be considered as a linear combination of symmetric and antisymmetric Lorentzian functions, where the symmetric and antisymmetric Lorentzian functions account for the in-phase and out-of-phase components of the RF wave.[64] In order to determine the effective anisotropy field from our field dependent TS curves, we fitted the line shapes for the TS curves with the following expression,[64]

$$\frac{\Delta\chi_T}{\chi_T} = \chi_{Sym} \frac{\left(\frac{\Delta H}{2}\right)^2}{\left(H_{dc}-H_K^{eff}\right)^2+\left(\frac{\Delta H}{2}\right)^2} + \chi_{Asym} \frac{\frac{\Delta H}{2}\left(H_{dc}-H_K^{eff}\right)}{\left(H_{dc}-H_K^{eff}\right)^2+\left(\frac{\Delta H}{2}\right)^2} + \chi_0 \quad (6)$$

where, χ_{Sym} and χ_{Asym} are the coefficients of symmetric and antisymmetric Lorentzian functions and χ_0 is the constant offset parameter. Figs. 8(a)-(d) demonstrate the fit of the unipolar TS curves using the Eqn. (6) for sample B at two selected temperatures for both IP and OOP configurations. It is evident that asymmetric contribution (asymmetry in the TS curve with respect to $\pm H_K^{eff}$ in the field range between 0 and $\pm H_{DC}^{sat}$) is more pronounced for the IP configuration at T = 300 K.

Next, we concentrate on the temperature dependence of $+H_K^{IP}$ and $+H_K^{OP}$ which we have associated with the effective anisotropy fields for the OOP and IP configurations obtained from the Lorentzian fits. Figs. 8(e)-(h) compare the temperature dependence of $+H_K^{OP}$ and $+H_K^{IP}$ for samples A-D, respectively, in the temperature range 40 K ≤ T ≤ 300 K, where $+H_K^{OP}$ and $+H_K^{IP}$ are represented by a solid red sphere and solid blue square, respectively. Complex temperature dependences of the IP and OOP effective anisotropy fields are noticeable for different samples. For sample A, the temperature dependence of both $+H_K^{OP}$ ($+H_K^{OP}(T)$) and $+H_K^{IP}$ ($+H_K^{IP}(T)$) follows almost the same trend; decrease from T = 300 K, followed by a broad maximum, and then again decrease with further reducing the temperature. Because of different magnitudes of $+H_K^{IP}$ and $+H_K^{OP}$ at different temperatures, there are some crossovers. In the temperature range 400 K ≤ T ≤ 300 K, there are three crossovers at T_{SR1}, T_{SR2}, and T_{SR3} which are indicated by arrows. For T

> T_{SR1}, $+H_K^{OP} \geq +H_K^{IP}$ whereas $+H_K^{OP} < +H_K^{IP}$ in the temperature range $T_{SR1} \leq T \leq T_{SR2}$ and again, $+H_K^{OP} > +H_K^{IP}$ for $T_{SR2} \leq T \leq T_{SR3}$. Below the third crossover at T_{SR3}, $+H_K^{IP} > +H_K^{OP}$ down to the lowest temperature.

Unlike the multiple spin reconfigurations in sample A, there is only one anisotropy crossover at $T = T_{SR}$ in the temperature range $40\ K \leq T \leq 300\ K$ for both samples B and C. For both samples B and C, $+H_K^{OP} > +H_K^{IP}$ for $T \geq T_{SR}$, but below the spin reorientation, $+H_K^{IP} > +H_K^{OP}$ down to the lowest temperature. Thus, these samples transform from a high-temperature IP anisotropy-dominated state to a low-temperature OOP anisotropy-dominated state below the spin reorientation transition. This is also in good agreement with our magnetometry data. There is another important feature: for sample B, both $+H_K^{OP}(T)$ and $+H_K^{IP}(T)$ undergo an abrupt decrease below 150 K and exhibit a broad minimum in the vicinity of its compensation temperature (≈ 70 K). This feature around the compensation point is stronger in $+H_K^{IP}(T)$ than in $+H_K^{OP}(T)$. On the other hand, for sample C, $+H_K^{IP}(T)$ shows a prominent dip but $+H_K^{OP}(T)$ shows a slope change around the compensation (≈ 200 K). At lower temperatures, $+H_K^{IP}(T)$ increases almost linearly and shows a broad hump around ~ 100 K, and $+H_K^{OP}(T)$ shows a broad minimum just below the compensation which is followed by a slight increase and then remains almost unaltered down to the lowest temperature. Unlike samples A-C, sample D does not show any spin reorientation in the measured temperature window and $+H_K^{IP} > +H_K^{OP}$ at all the temperatures. Moreover, both $+H_K^{OP}(T)$ and $+H_K^{IP}(T)$ exhibit a broad maximum at ≈ 150 K.

To explain the anomalous behavior of $H_K^{IP}(T)$ and $H_K^{OP}(T)$ in the vicinity of T_{Comp}, let us start from the energy landscape of the system. For simplicity, we consider that the $Fe_{100-x}Gd_x$

system is composed of Gd-enriched and Fe-enriched phases which are antiferromagnetically coupled by inter-subnetwork exchange interaction. A schematic representation of different orientations of the subnetwork magnetizations associated with the Gd-enriched (M_{Gd}^{Rich}) and Fe-enriched (M_{Fe}^{Rich}) domains relative to the applied bias field (H_{DC}) is shown in Fig. 6(c). In the absence of H_{DC}, both M_{Gd}^{Rich} and M_{Fe}^{Rich} prefer an antiparallel alignment along the magnetic easy axis. When H_{DC} is applied at an angle ϕ with respect to the easy axis, both M_{Gd}^{Rich} and M_{Fe}^{Rich} undergo slight deviation from the antiparallel alignment by angles θ_{Gd} and θ_{Fe}, respectively. Since the Gd moment dominates at low temperatures, we assume that $M_{Gd}^{Rich}>M_{Fe}^{Rich}$. In the framework of the Mean-field model, the energy density for this ferrimagnetic system can be expressed as,[60,65]

$$E = \left[-\mu_0 H_{DC} M_{Gd}^{Rich} cos(\emptyset - \theta_{Gd}) + \mu_0 H_{DC} M_{Fe}^{Rich} cos(\emptyset - \theta_{Fe})\right] + [K_1^{Gd} sin^2\theta_{Gd} + K_1^{Fe} sin^2\theta_{Fe}] - \left[\lambda_{Gd-Fe}^{inh} M_{Gd}^{Rich}\, M_{Fe}^{Rich} cos(\theta_{Gd} - \theta_{Fe})\right], \quad (7)$$

where, K_1^{Gd} and K_1^{Fe} are the first-order anisotropy constants associated with the Gd-enriched and Fe-enriched phases, respectively and λ_{Gd-Fe}^{inh} is the inter-subnetwork Weiss field constant. In Eqn. (7), the first, second, third, and fourth terms within the square brackets represent the Zeeman energy, the anisotropy energy, and the inter-sublattice exchange energy. Following the approach of Sarkis et al.,[60] and Drzazga et.[65] al., the effective anisotropy constant for our compensated ferrimagnetic $Fe_{100-x}Gd_x$ system can be expressed as,

$$K_{eff} = M_S^2 \left[\frac{\lambda_{Gd-Fe}^{inh} M_{Gd}^{Rich} M_{Fe}^{Rich} \{K_1^{Gd} + K_1^{Fe}\} + 2K_1^{Gd} K_1^{Fe}}{2\left[K_1^{Gd}\left(M_{Fe}^{Rich}\right)^2 + K_1^{Fe}\left(M_{Gd}^{Rich}\right)^2\right] + \lambda_{Gd-Fe}^{inh} M_{Gd}^{Rich} M_{Fe}^{Rich} M_S^2}\right]. \quad (8)$$

Here, $M_S = \left[M_{Gd}^{Rich} - M_{Fe}^{Rich}\right]$ is the net magnetization of the $Fe_{100-x}Gd_x$ system. Eqn. (8) suggests that K_{eff} is strongly dependent on the sublattice magnetizations, sublattice anisotropies, and inter-sublattice exchange interaction. Most importantly, Eqn. (8) indicates that K_{eff} become zero at the compensation point, as $M_S = \left[M_{Gd}^{Rich} - M_{Fe}^{Rich}\right] = 0$, which explains the minimum/dip observed in $H_K^{OP}(T)$ and $+H_K^{IP}(T)$ at T_{Comp} for both samples B and C. Minimum in the effective anisotropy constant/field around T_{Comp} is expected in rare-earth (RE) – transition metal (TM) based compensated ferrimagnets,[60,65-67] which is generally explained in terms of canting of the sublattice magnetizations near T_{Comp}.

Finally, it is known that the microstructure and hence, the internal planar stress in physical vapor deposited/sputtered films are sensitive to the deposition conditions, e.g., the partial pressure of Ar (P_{Ar}).[68,69] The orientation of the magnetic easy axis strongly depends on the internal stress of the film and hence, dependent on the Ar partial pressure. For FeGd amorphous films, it is reported that the internal planar stress is compressive at $P_{Ar} = 6 \times 10^{-2}$ Torr which transforms to tensile at $P_{Ar} = 10 \times 10^{-2}$ Torr.[69] Nevertheless, PMA is significant for the films with compressive strain. This internal stress induced PMA can be avoided by using a lower Ar partial pressure while deposition. The Ar partial pressure during the deposition of our FeGd films was 6×10^{-3} Torr which is almost an order of magnitude lower than that for the films with compressive strain. Moreover, influence of internal stress on the uniaxial anisotropy is the minimum for the Gd atomic percent range $22 \leq x \leq 28$,[69] and in our present study, we are dealing with the composition range $22.8 \leq x \leq 26.2$ in $Fe_{100-x}Gd_x$. So, the stress induced anisotropy in our $Fe_{100-x}Gd_x$ films is negligible and the origin of PMA observed in these films is intrinsic. Our study concerning the precise determination of effective anisotropy fields as a function of temperature using the TS technique for both IP and OOP configurations is new among the RE-TM based systems and our TS technique would pave the way for the development of novel spintronic devices with excellent PMA.

V. CONCLUSIONS

In summary, we have used the DC magnetometry and RF transverse susceptibility measurements to carefully examine the temperature evolution of in-plane and out-of-plane effective anisotropy fields in ferrimagnetic $Fe_{100-x}Gd_x$ amorphous films by varying the Gd concentration. The compensation temperature moves to a higher temperature with increasing Gd concentration. We suggest that the $Fe_{100-x}Gd_x$ system is phase segregated into Fe-enriched and Gd-enriched regions. A two-step reversal behavior emerges in the OOP M(H) loop near compensation, which we attribute to the sequential magnetization reversals of Fe-enriched and Gd-enriched domains. Since the Gd-enriched domains prefer OOP anisotropy, this two-step magnetization reversal suggests a temperature-induced transformation from IP to OOP spin configuration below a certain temperature. Our RF transverse susceptibility measurements indicate that the effective magnetic anisotropy for OOP configuration dominates over IP configuration (*i.e.*, $H_K^{IP} > H_K^{OP}$) below a certain temperature which validates the occurrence of spin reorientation. Both IP and OOP anisotropy fields determined from our TS measurement exhibit a minimum around the compensation which has been supported by the Stoner-Wohlfarth model. Thus, the presence of competing magnetic anisotropies and spin reorientations as revealed by our TS data together with the magnetometry results potentially point towards the existence of phase separated regions with distinct magnetic easy axes in our amorphous ferrimagnetic $Fe_{100-x}Gd_x$ films.

VI. ACKNOWLEDGEMENTS

HS acknowledges support from USF Department of Energy, Office of Basic Energy Sciences, Division of Materials Science and Engineering under Award No. DE-FG02-07ER46438. JS and DAA acknowledge support of the National Science Foundation under Grant No. ECCS-1952957.

Figure Captions

FIG. 1(a)-(d) Temperature dependence of in-plane magnetization, *M*(*T*) of the $Fe_{100-x}Gd_x$ films with different Gd concentrations (samples A-D, respectively) measured in a magnetic field of $\mu_0 H$ = 1 T in the field-cooled cooling mode.

FIG. 2(a)-(d) In-plane (IP) and out-of-plane (OOP) M(H) loops at *T* = 300 K for the films A - D, respectively and (e)-(h) IP and OOP M(H) measured at *T* = 10 K for the same samples; insets show expanded view of the low field hysteresis behavior of the MH loops.

FIG. 3(a)-(d) The OOP M(H) loops in the temperature range: $10 \leq T \leq 300$ K for samples A-D, respectively.

FIG. 4(a) OOP M(H) loops at T = 75 and 100 K for sample B, (b) OOP M(H) at T = 200 K for sample C, and (c) Expanded view of OOP M(H) loop for sample B at T = 75 K for better visibility of the spin-flop (SF) transition. The spin-flop transition field and coercive field are indicated by H_{SF} and H_C, respectively in the figure.

FIG. 5(a)-(d) Temperature dependence of saturation magnetization (M_S) normalized w.r.t its value at T = 300 K (M_S/M_S^{300K}) on the left *y*-scale and the ratio of remanent magnetization (M_R) and M_S on the right y-scale obtained from the OOP M(H) loops for the samples A-D, respectively, (e)-(h) coercivity (H_C) of the OOP M(H) loops as a function of temperature for samples A-D, respectively. Note that the magnetization of the saturated ferrimagnetic macro-spins is indicated as the saturation magnetization, M_S throughout the manuscript.

FIG. 6(a) 3D polar representation of different orientations of the magnetization vector (M_S), DC, and RF magnetic fields relative to the magnetic easy axis of a single domain particle with uniaxial magnetic anisotropy fulfilling the experimental conditions of a typical TS measurement, (b) schematic of our TS measurement geometry for IP and OOP configurations, and (c) schematic representation of different orientations of Gd sublattice magnetization (M_{Gd}) and Fe sublattice magnetization (M_{Fe}) relative to the applied bias field (H_{DC}).

FIG. 7 IP (left-y scale) and OOP (right y-scale) TS data for samples A-D, respectively for bipolar field scans ($+H_{DC}^{sat} \rightarrow -H_{DC}^{sat} \rightarrow +H_{DC}^{sat}$) at (a)-(d) T = 300 K, (e)-(h) T = 200 K (close to the compensation for sample C), and (i)-(l) T = 60 K (close to the compensation for sample B).

FIG. 8(a)-(d) Lorentzian fits to the OOP and IP TS line shapes for sample B at T = 300 K ((a) and (b)) and T = 60 K ((c) and (d)). Temperature dependence of IP anisotropy field ($+H_K^{IP}$) and OOP anisotropy field ($+H_K^{OP}$) for the samples A-D are shown in (e)-(h), respectively.

List of Figures

FIG. 1

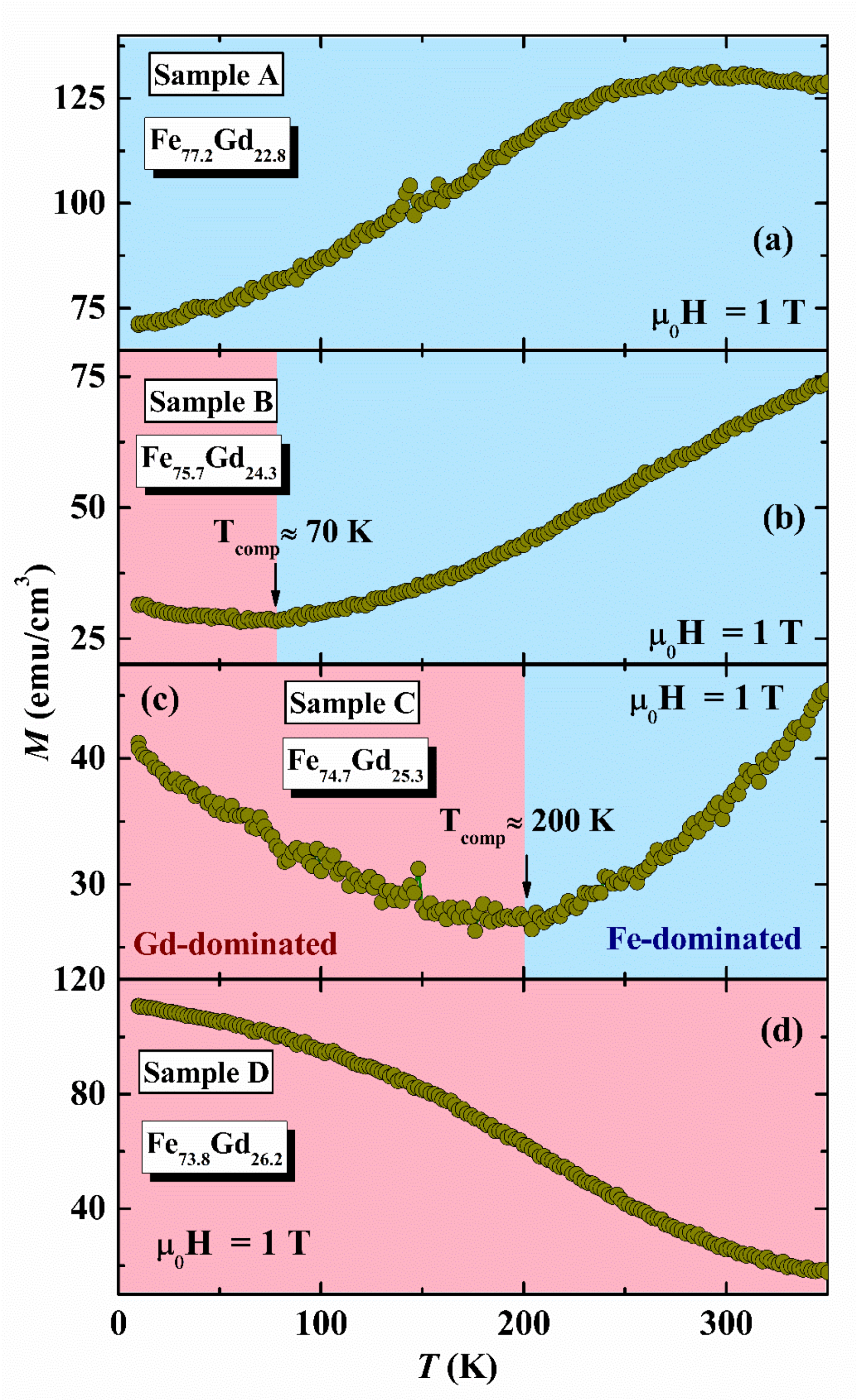

FIG. 2

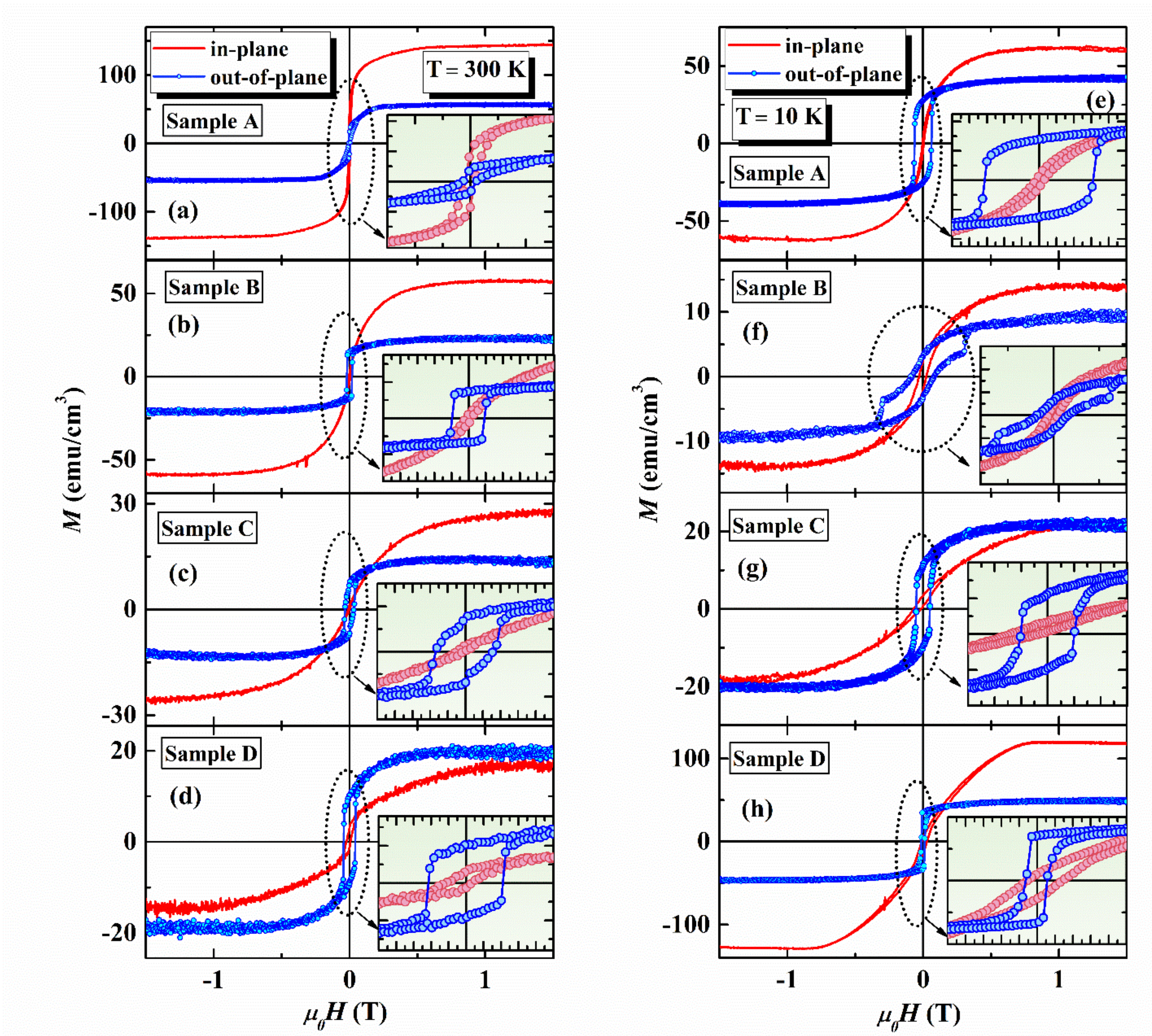

in-plane
out-of-plane
T = 300 K
Sample A
(a)
Sample B
(b)
Sample C
(c)
Sample D
(d)
M (emu/cm3)
μ0H (T)
T = 10 K
(e)
Sample A
Sample B
(f)
Sample C
(g)
Sample D
(h)
M (emu/cm3)
μ0H (T)

FIG. 3

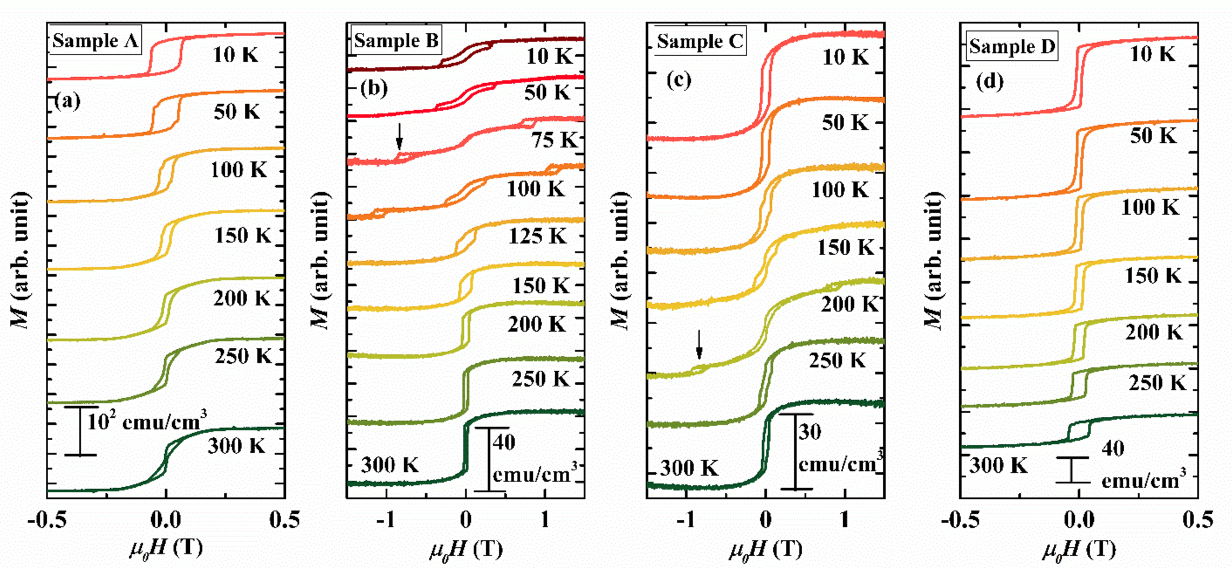

Sample A
(a)
10 K
50 K
100 K
150 K
200 K
250 K
300 K
10^2 emu/cm^3
M (arb. unit)
-0.5
0.0
0.5
μ_0H (T)
Sample B
(b)
10 K
50 K
75 K
100 K
125 K
150 K
200 K
250 K
300 K
40 emu/cm^3
M (arb. unit)
-1
0
1
μ_0H (T)
Sample C
(c)
10 K
50 K
100 K
150 K
200 K
250 K
300 K
30 emu/cm^3
M (arb. unit)
-1
0
1
μ_0H (T)
Sample D
(d)
10 K
50 K
100 K
150 K
200 K
250 K
300 K
40 emu/cm^3
M (arb. unit)
-0.5
0.0
0.5
μ_0H (T)

FIG. 4

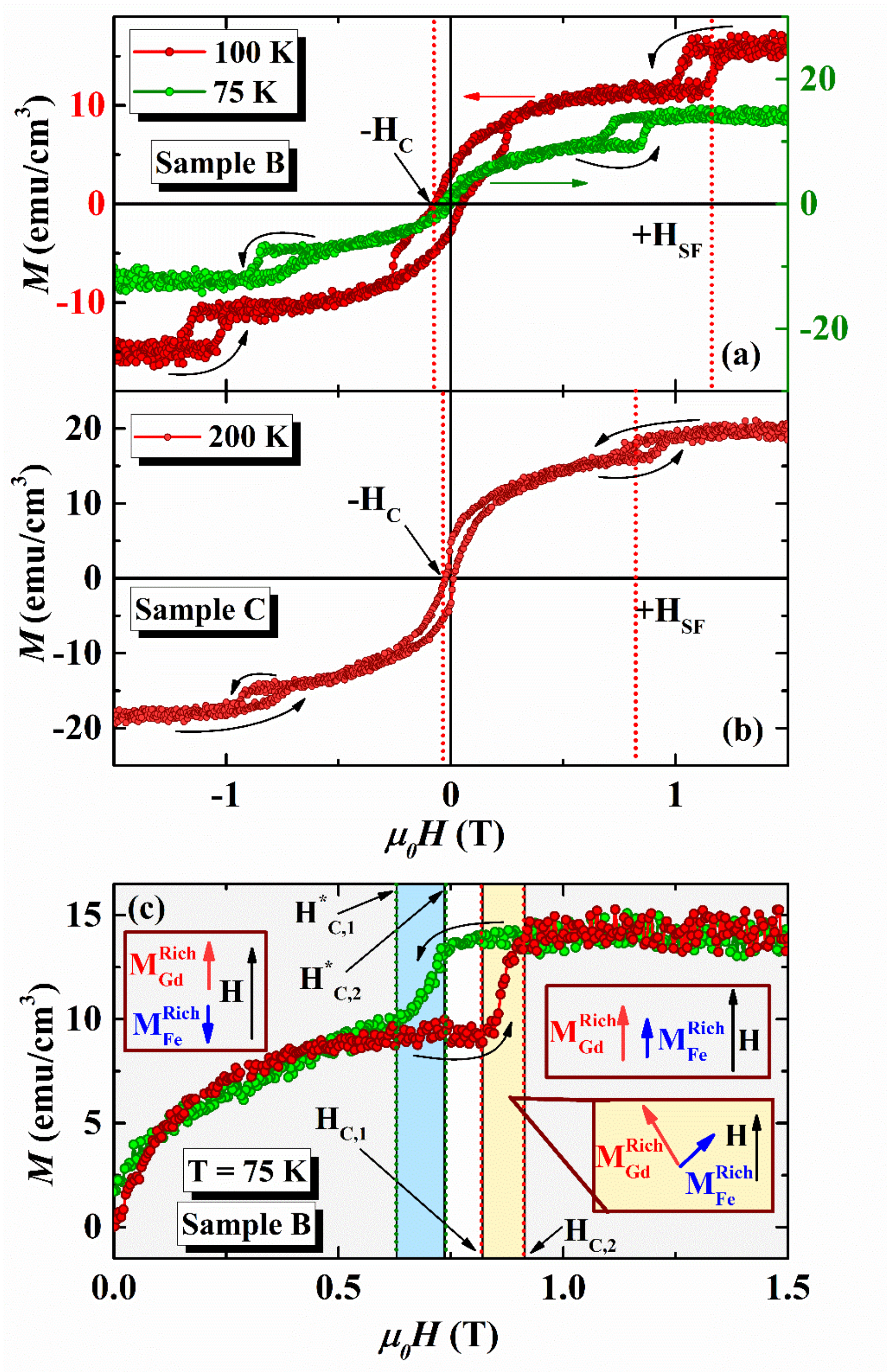
100 K
75 K
Sample B
-H$_C$
+H$_{SF}$
M (emu/cm^3)
(a)
200 K
Sample C
(b)
$\mu_0 H$ (T)
(c)
H$^*_{C,1}$
H$^*_{C,2}$
H$_{C,1}$
H$_{C,2}$
M$^{Rich}_{Gd}$
M$^{Rich}_{Fe}$
H
T = 75 K

FIG. 5

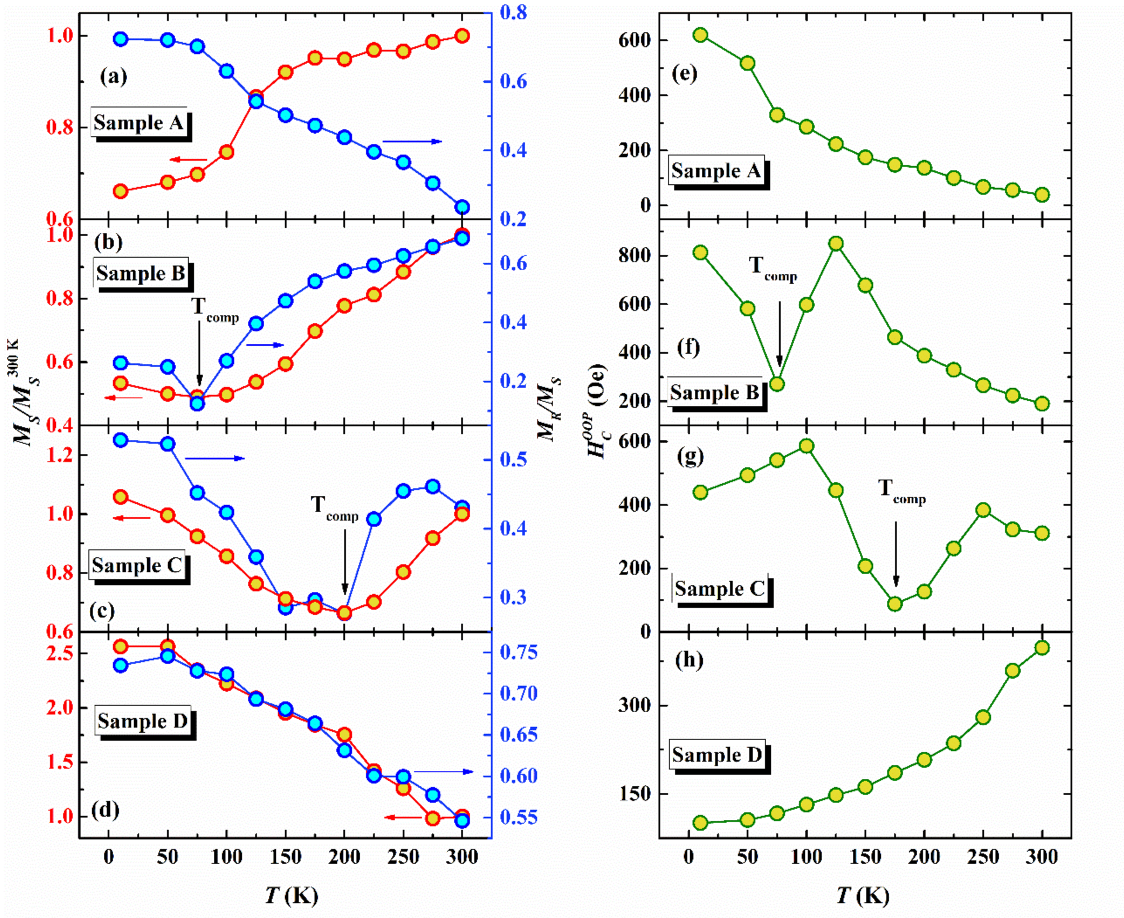
(a)
Sample A
(b)
Sample B
T comp
(c)
Sample C
T comp
(d)
Sample D
(e)
Sample A
(f)
T comp
Sample B
(g)
T comp
Sample C
(h)
Sample D
$M_S/M_S^{300\ K}$
M_R/M_S
H_C^{OOP} (Oe)
T (K)
T (K)

FIG. 6

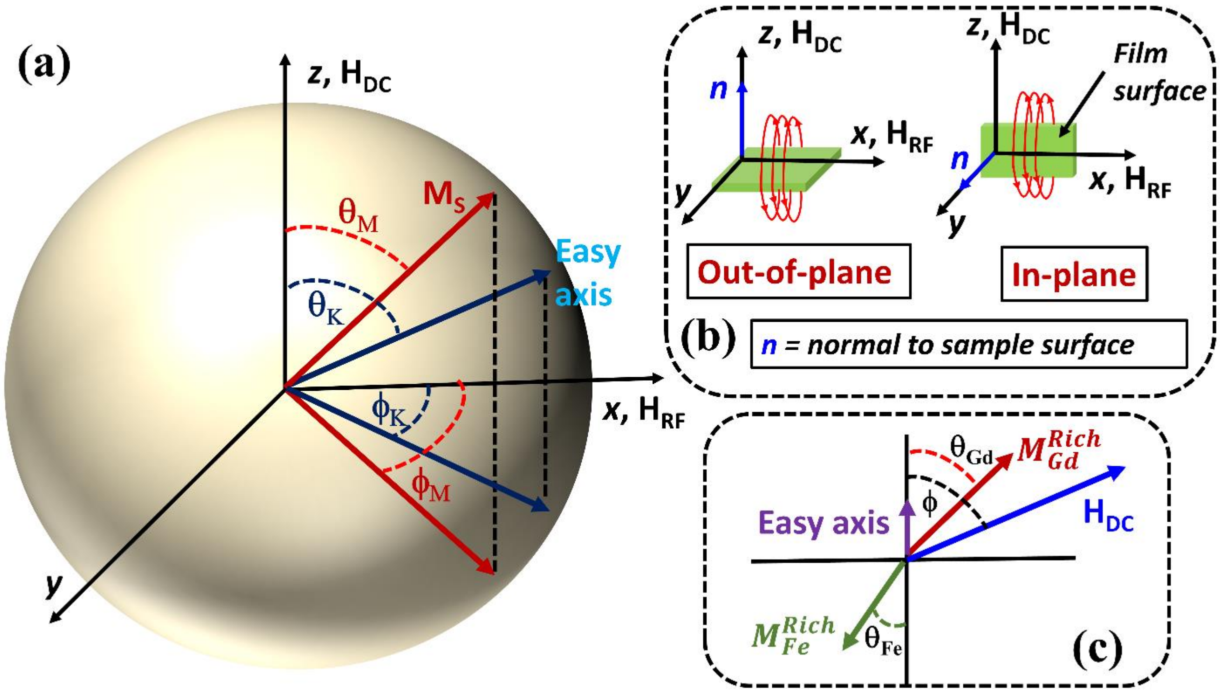
(a)
z, H_{DC}
M_S
θ_M
θ_K
Easy axis
ϕ_K
ϕ_M
x, H_{RF}
y
z, H_{DC}
n
x, H_{RF}
y
Out-of-plane
z, H_{DC}
Film surface
n
x, H_{RF}
y
In-plane
(b)
n = normal to sample surface
θ_{Gd}
M_{Gd}^{Rich}
ϕ
Easy axis
H_{DC}
M_{Fe}^{Rich}
θ_{Fe}
(c)

FIG. 7

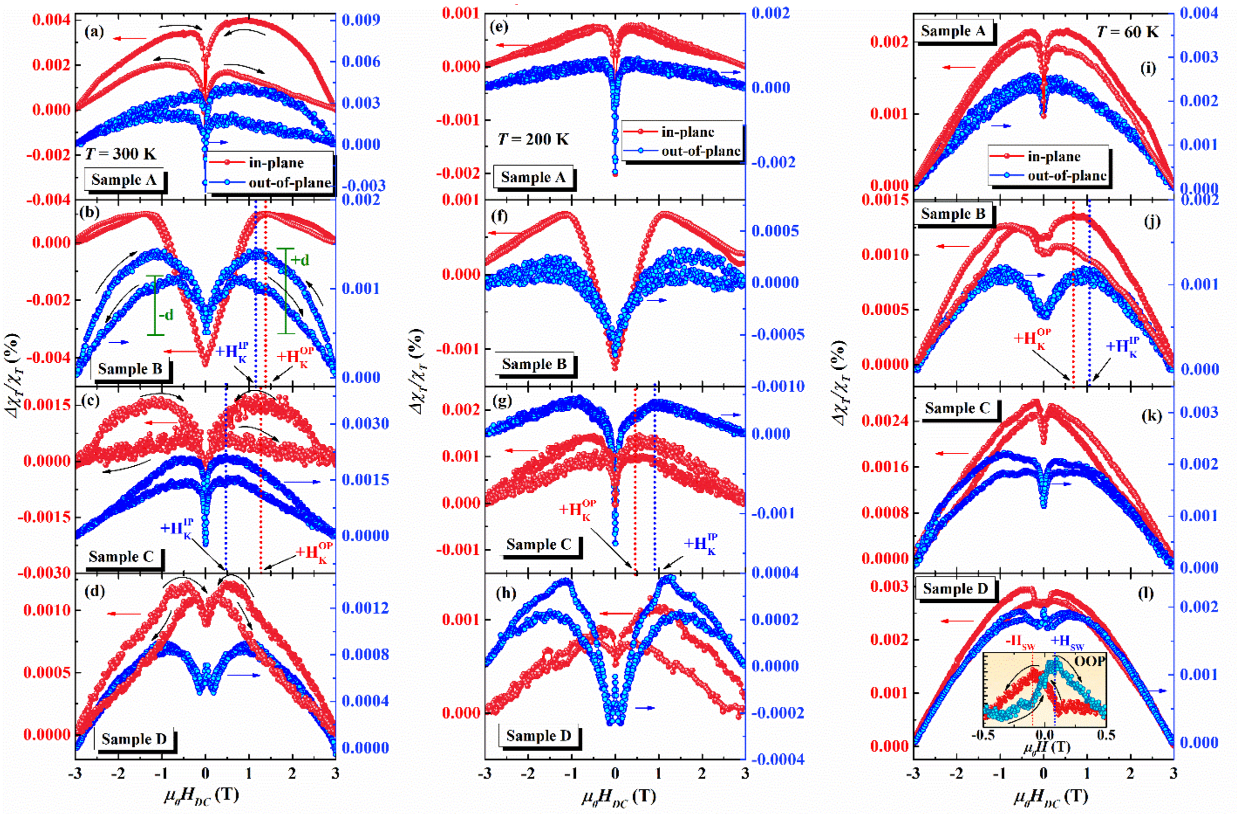

(a)
T = 300 K
Sample A
in-plane
out-of-plane
(b)
Sample B
+d
-d
$+H_K^{IP}$
$+H_K^{OP}$
(c)
Sample C
(d)
Sample D
(e)
T = 200 K
(f)
(g)
(h)
(i)
T = 60 K
(j)
(k)
(l)
$-H_{SW}$
$+H_{SW}$
OOP
$\mu_0 H$ (T)
$\Delta\chi_T/\chi_T$ (%)
$\mu_0 H_{DC}$ (T)

FIG. 8

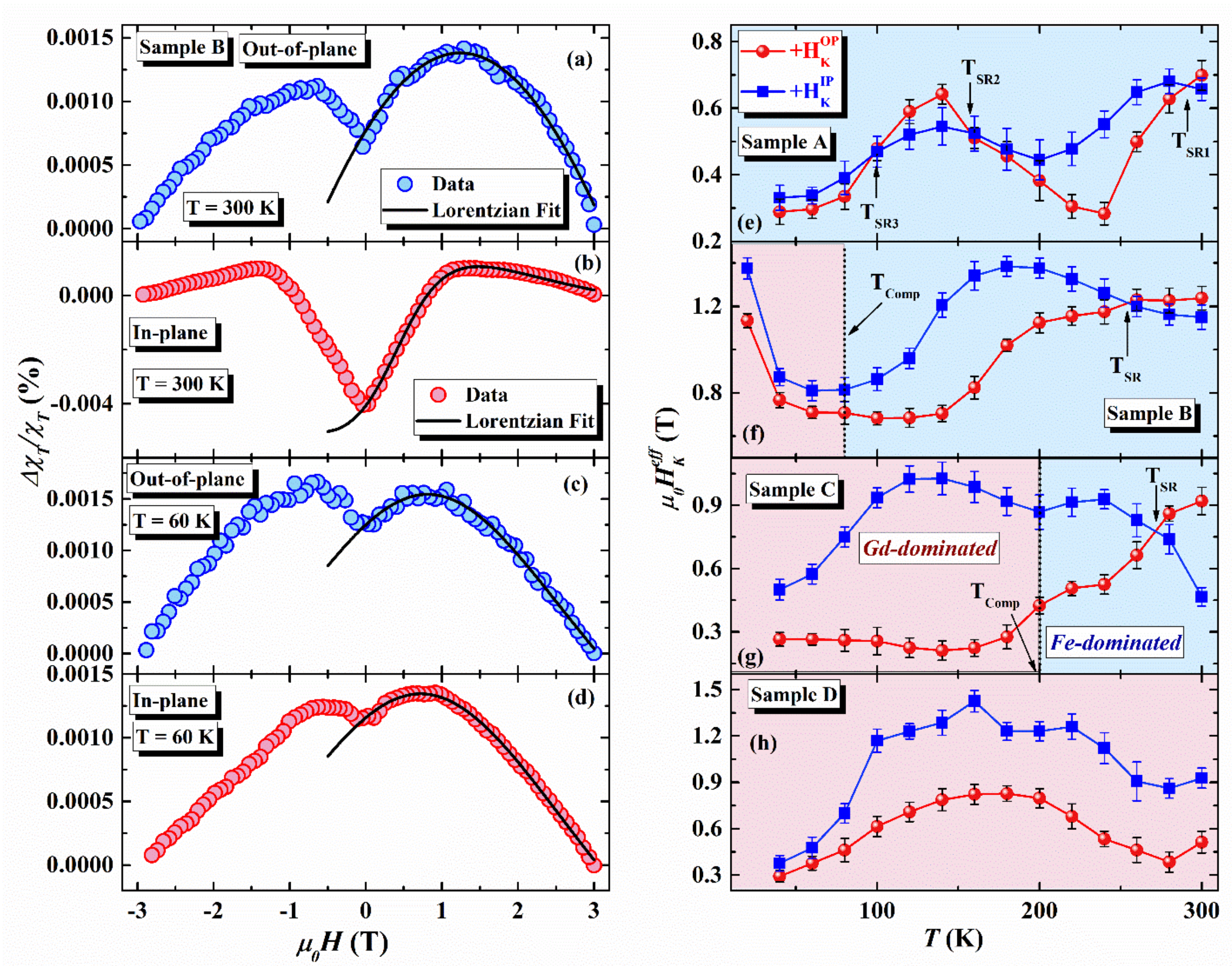

Sample B
Out-of-plane
(a)
T = 300 K
Data
Lorentzian Fit
(b)
In-plane
T = 300 K
Data
Lorentzian Fit
Out-of-plane
(c)
T = 60 K
In-plane
(d)
T = 60 K
Δχ_T/χ_T (%)
μ_0H (T)
+H_K^OP
+H_K^IP
T_SR2
Sample A
T_SR1
T_SR3
(e)
T_Comp
T_SR
Sample B
(f)
Sample C
T_SR
Gd-dominated
T_Comp
Fe-dominated
(g)
Sample D
(h)
μ_0H_K^eff (T)
T (K)

References

[1] P. Hansen, C. Clausen, G. Much, M. Rosenkranz, and K. Witter, J. Appl. Phys. **66**, 756 (1989).

[2] S. Mangin, M. Gottwald, C. Lambert, D. Steil, V. Uhlíř, L. Pang, M. Hehn, S. Alebrand, M. Cinchetti, and G. Malinowski, Nature Materials **13**, 286 (2014).

[3] L. Le Guyader, S. El Moussaoui, M. Buzzi, M. Savoini, A. Tsukamoto, A. Itoh, A. Kirilyuk, T. Rasing, F. Nolting, and A. V. Kimel, Physical Review B **93**, 134402 (2016).

[4] B. Dai, T. Kato, S. Iwata, and S. Tsunashima, IEEE Trans. Magn. **48**, 3223 (2012).

[5] T. Ostler, J. Barker, R. Evans, R. Chantrell, U. Atxitia, O. Chubykalo-Fesenko, S. El Moussaoui, L. Le Guyader, E. Mengotti, and L. Heyderman, Nature Communications **3**, 1 (2012).

[6] P. Hansen, J. Appl. Phys. **63**, 2364 (1988).

[7] N. Roschewsky, C.-H. Lambert, and S. Salahuddin, Physical Review B **96**, 064406 (2017).

[8] R. Mishra, J. Yu, X. Qiu, M. Motapothula, T. Venkatesan, and H. Yang, Phys. Rev. Lett. **118**, 167201 (2017).

[9] J. Kim, D. Lee, K.-J. Lee, B.-K. Ju, H. C. Koo, B.-C. Min, and O. Lee, Scientific Reports **8**, 1 (2018).

[10] Z. Zheng, Y. Zhang, X. Feng, K. Zhang, J. Nan, Z. Zhang, G. Wang, J. Wang, N. Lei, and D. Liu, Physical Review Applied **12**, 044032 (2019).

[11] R. Schneider, M. Fix, J. Bensmann, S. Michaelis de Vasconcellos, M. Albrecht, and R. Bratschitsch, Appl. Phys. Lett. **115**, 152401 (2019).

[12] L. Caretta, M. Mann, F. Büttner, K. Ueda, B. Pfau, C. M. Günther, P. Hessing, A. Churikova, C. Klose, and M. Schneider, Nature Nanotechnology **13**, 1154 (2018).

[13] S. Woo, K. M. Song, X. Zhang, Y. Zhou, M. Ezawa, X. Liu, S. Finizio, J. Raabe, N. J. Lee, and S.-I. Kim, Nature Communications **9**, 1 (2018).

[14] R. Taylor and A. Gangulee, Physical Review B **22**, 1320 (1980).

[15] T. A. Ostler, R. F. Evans, R. W. Chantrell, U. Atxitia, O. Chubykalo-Fesenko, I. Radu, R. Abrudan, F. Radu, A. Tsukamoto, and A. Itoh, Physical Review B **84**, 024407 (2011).

[16] R. Taylor and A. Gangulee, J. Appl. Phys. **48**, 358 (1977).

[17] R. Camley, Physical Review B **35**, 3608 (1987).

[18] W. He, H.-L. Liu, H.-Y. Wu, J.-W. Cai, and Z.-H. Cheng, Appl. Phys. Lett. **106**, 042401 (2015).

[19] Y. Suzuki, S. Takayama, F. Kirino, and N. Ohta, IEEE Trans. Magn. **23**, 2275 (1987).
[20] W. Meiklejohn, J. Appl. Phys. **33**, 1328 (1962).
[21] H. Fu and M. Mansuripur, Physical Review B **45**, 7188 (1992).
[22] H. Fu, M. Mansuripur, and P. Meystre, Phys. Rev. Lett. **66**, 1086 (1991).
[23] V. Harris, K. Aylesworth, B. Das, W. Elam, and N. Koon, Phys. Rev. Lett. **69**, 1939 (1992).
[24] E. Kirk, C. Bull, S. Finizio, H. Sepehri-Amin, S. Wintz, A. Suszka, N. Bingham, P. Warnicke, K. Hono, and P. Nutter, Physical Review Materials **4**, 074403 (2020).
[25] M. Urner-Wille and K. Witter, Journal of Magnetism and Magnetic Materials **13**, 77 (1979).
[26] Y. Mimura, N. Imamura, and T. Kobayashi, J. Appl. Phys. **47**, 368 (1976).
[27] E. Jesenská, T. Ishibashi, L. Beran, M. Pavelka, J. Hamrle, R. Antoš, J. Zázvorka, and M. Veis, Scientific reports **9**, 1 (2019).
[28] J. Coey, J. Appl. Phys. **49**, 1646 (1978).
[29] S. Ohbayashi, M. Harada, M. Nawate, M. Ohkoshi, S. Honda, and T. Kusuda, IEEE Translation Journal on Magnetics in Japan **2**, 340 (1987).
[30] J. Orehotsky and K. Schröder, J. Appl. Phys. **43**, 2413 (1972).
[31] T. Morishita, Y. Togami, and K. Tsushima, J. Phys. Soc. Jpn. **54**, 37 (1985).
[32] Y. Mimura, N. Imamura, T. Kobayashi, A. Okada, and Y. Kushiro, J. Appl. Phys. **49**, 1208 (1978).
[33] Y. Choi, D. Haskel, A. Cady, J. Lang, D. Lee, G. Srajer, J. Jiang, and S. Bader, Physical Review B **73**, 174401 (2006).
[34] A. Drovosekov, A. Savitsky, D. Kholin, N. Kreines, V. Proglyado, M. Makarova, E. Kravtsov, and V. Ustinov, Journal of Magnetism and Magnetic Materials **475**, 668 (2019).
[35] R. Camley and D. Tilley, Physical Review B **37**, 3413 (1988).
[36] Y. Kamiguchi, H. Fujimori, and M. Motokawa, J. Phys. Soc. Jpn. **61**, 3721 (1992).
[37] K. Okamoto and N. Miura, Physica B: Condensed Matter **155**, 259 (1989).
[38] O. Inyang, A. Rafiq, C. Swindells, S. Ali, and D. Atkinson, Scientific Reports **10**, 1 (2020).
[39] S. Mondal, A. Talapatra, J. A. Chelvane, J. R. Mohanty, and A. Barman, Physical Review B **100**, 054436 (2019).
[40] A. Talapatra, J. A. Chelvane, and J. Mohanty, Journal of Magnetism and Magnetic Materials **448**, 360 (2018).

[41] M. Krupinski, J. Hintermayr, P. Sobieszczyk, and M. Albrecht, Physical Review Materials **5**, 024405 (2021).

[42] See Supplemental Material at for X-ray reflectivity and High-angle X-ray diffraction data.

[43] A. Drovosekov, N. Kreines, A. Savitsky, E. Kravtsov, D. Blagodatkov, M. Ryabukhina, M. Milyaev, V. Ustinov, E. Pashaev, and I. Subbotin, Journal of Experimental and Theoretical Physics **120**, 1041 (2015).

[44] H. Srikanth, J. Wiggins, and H. Rees, Rev. Sci. Instrum. **70**, 3097 (1999).

[45] A. Aharoni, E. H. Frei, S. Shtrikman, and D. Treves, Bull. Res. Counc. Isr., Sect. A: Math., Phys. Chem. **6A**, 215 (1957).

[46] A. Hoare, R. Chantrell, W. Schmitt, and A. Eiling, J. Phys. D: Appl. Phys. **26**, 461 (1993).

[47] R. Matarranz, M. Contreras, G. Pan, B. Presa, J. Corrales, and J. Calleja, J. Appl. Phys. **99**, 08Q504 (2006).

[48] R. P. Madhogaria, C.-M. Hung, B. Muchharla, A. T. Duong, R. Das, P. T. Huy, S. Cho, S. Witanachchi, H. Srikanth, and M.-H. Phan, Physical Review B **103**, 184423 (2021).

[49] A. Stanciu, G. Schinteie, A. Kuncser, N. Iacob, L. Trupina, I. Ionita, O. Crisan, and V. Kuncser, Journal of Magnetism and Magnetic Materials **498**, 166173 (2020).

[50] H. Basumatary, J. A. Chelvane, D. S. Rao, A. Talapatra, J. Mohanty, D. Kumar, V. Singh, S. Kamat, and R. Ranjan, J. Alloys Compd. **869**, 159571 (2021).

[51] A. E. Clark and E. Callen, J. Appl. Phys. **39**, 5972 (1968).

[52] A. Drovosekov, D. Kholin, and N. Kreinies, Journal of Experimental and Theoretical Physics **131**, 149 (2020).

[53] A. Paduan-Filho, C. Becerra, and F. Palacio, Physical Review B **43**, 11107 (1991).

[54] M. Date and K. Nagata, J. Appl. Phys. **34**, 1038 (1963).

[55] F. B. Anderson and H. B. Callen, Phys. Rev. **136**, A1068 (1964).

[56] F. Keffer and H. Chow, Phys. Rev. Lett. **31**, 1061 (1973).

[57] K. Umadevi, S. Bysakh, J. A. Chelvane, S. Kamat, and V. Jayalakshmi, J. Alloys Compd. **663**, 430 (2016).

[58] A. Talapatra, J. A. Chelvane, B. Satpati, S. Kumar, and J. Mohanty, J. Alloys Compd. **774**, 1059 (2019).

[59] J. Becker, A. Tsukamoto, A. Kirilyuk, J. Maan, T. Rasing, P. Christianen, and A. Kimel, Phys. Rev. Lett. **118**, 117203 (2017).

[60] A. Sarkis and E. Callen, Physical Review B **26**, 3870 (1982).

[61] L. Spinu, I. Dumitru, A. Stancu, and D. Cimpoesu, Journal of magnetism and magnetic materials **296**, 1 (2006).

[62] D. Cimpoesu, A. Stancu, and L. Spinu, Physical Review B **76**, 054409 (2007).

[63] V. Ivanshin, J. Deisenhofer, H.-A. K. Von Nidda, A. Loidl, A. Mukhin, A. Balbashov, and M. V. Eremin, Physical Review B **61**, 6213 (2000).

[64] M. Harder, Z. Cao, Y. Gui, X. Fan, and C.-M. Hu, Physical Review B **84**, 054423 (2011).

[65] Z. Drzazga and M. Drzazga, Journal of magnetism and magnetic materials **65**, 21 (1987).

[66] A. Ermolenko, IEEE Trans. Magn. **12**, 992 (1976).

[67] Z. Drzazga, Physica B+ C **130**, 305 (1985).

[68] J. A. Thornton and D. Hoffman, Thin Solid Films **171**, 5 (1989).

[69] H. Takagi, S. Tsunashima, S. Uchiyama, and T. Fujii, J. Appl. Phys. **50**, 1642 (1979).